Tunable nonlocal metasurfaces based on graphene for analogue optical computation

IRYNA KHODASEVYCH,[1] LUKAS WESEMANN,[2] ANN ROBERTS,[2] AND FRANCESCA IACOPI[1*]

[1]*ARC Centre of Excellence for Transformative Meta-Optical Systems, School of Electrical and Data Engineering, Faculty of Engineering and IT, University of Technology Sydney, Broadway, NSW 2007, Australia*

[2]*ARC Centre of Excellence for Transformative Meta-Optical Systems, School of Physics, The University of Melbourne, Victoria 3010, Australia*

**francesca.iacopi@uts.edu.au*

Abstract: Meta-optical devices have recently emerged as ultra-compact candidates for real-time computation in the spatial domain. The use of meta-optics for applications in image processing and wavefront sensing could enable an order of magnitude increase in processing speed and data throughput, while simultaneously drastically reducing the footprint of currently available solutions to enable miniaturisation. Most research to date has focused on static devices that can perform a single operation. Dynamically tunable devices, however, offer increased versatility. Here we propose graphene covered subwavelength silicon carbide gratings as electrically tunable optical computation and image processing devices at mid-infrared wavelengths.

1. Introduction

Capturing and processing spatially resolved electromagnetic information underpins important applications in fields including biological research, medical diagnostics, machine vision and remote sensing. The near- and mid-infrared spectral regions are specifically attractive for obtaining insights beyond more readily available data at visible wavelengths using long wave infrared spectrometers [1]. Spatially resolved data at infrared wavelengths is for example used in plant tissue discrimination and biomolecule detection [2], cancer cell research [3], machine vision applications including real time data processing for autonomous vehicles [4] as well as thermal satellite imaging [5]. Today most of these applications rely on capturing spatial information in the form of intensity using conventional photodetectors, and subsequently applying digital processing. While these computations can be efficiently performed with modern algorithms in most cases, applications that generate large amounts of high-resolution data can push current electronic systems to their limits and use significant amounts of time and energy [6].

Nonlocal meta-optical devices based on thin-films [7–10], sub-wavelength gratings [11–13], metasurfaces [14, 15] and photonic crystals [16] have recently emerged as potential ultra-compact candidates to perform object/image plane all-optical analogue computation on images and other spatial information in real-time [17]. In contrast to conventional spatial frequency filters, that require transformation into Fourier space via lenses or lens-like elements, these types of devices enable direct manipulation of the Fourier content of a wavefield via a nonlocal process sometimes referred to as the "Green's function approach" [18]. These devices can be engineered to perform specific spatial mathematical operations on a transmitted or reflected wavefield in real-time. The replacement of digital algorithms with such ultra-compact, all-optical processing solutions could in some cases eliminate the data processing time and energy

required for computationally intensive high-speed applications. In addition to this, some types of spatial information processing rely on information that is not captured by conventional photodetectors, such as polarisation and phase, and usually require additional optical components to extract this information from an optical wavefield. These underpin for example biological phase-imaging [21] as well as wavefront sensing for applications in astronomy [20]. The bulky nature of conventional approaches to all-optical phase-visualisation such as Zernike microscopy or differential interference contrast (DIC) imaging recently motivated the development of ultra-compact approaches to enable low cost portable devices. Meta-optical solutions have been demonstrated to enable real-time extraction of phase-information in the visible part of the spectrum [7, 15] including for biological phase imaging [13, 14] and wavefront sensing [21].

Most of the research in this field until now has been directed towards the investigation of photonic devices that can perform a specific spatial mathematical operation, such first- and second order differentiation for the demonstration of edge-detection and phase visualisation. Subwavelength gratings supporting guided mode resonances have previously been investigated as all-optical spatial differentiators [11, 12]. We believe that for the successful integration of meta-optical computation devices into future ultra-compact systems, versatile processing capabilities will be crucial. These could for example include switching back and forth between transparency and edge detection modes. While there has been significant effort directed towards engineering meta-optical devices for tunable absorption and wavefront control based on phase-change materials and MEMS [22–25], tunable meta-optical devices for all-optical spatial computation have only recently attracted attention [26–30].

Graphene has gained popularity as an enabling material for nanophotonic devices due to its exceptional optical and electro-optical properties spanning the THz to the mid-infrared spectral range [31-36]. The possibility of adjusting the Fermi level E_f of graphene through electric gating permits shifting the resonances of meta-optical devices thereby enabling tuning of the optical response [32, 37, 38]. While other materials can be used for tuning, such as doped semiconductors and conducting oxides, their use has been limited to visible and near-infrared operation wavelengths with only a few attempts to adapt them to the mid-infrared. They require high carrier concentrations $\sim 10^{21}$ cm^{-3} adjusted at the fabrication stage in order to achieve an effective modulation level [39, 40]. However, this reduces transmission in the mid-infrared, as shown for doped Si [41] and indium tin oxide [42], due to the increasingly negative permittivity and growing extinction coefficient [43-45]. While a high extinction coefficient is suitable for absorption modulation, high transmission is essential for imaging. Fast picosecond tuning in the near-infrared with phase change materials, such as vanadium dioxide, has been demonstrated via laser pumping [46], however, it involves a more complex experimental set-up. Electrical tuning also remains in the nanosecond range, as it relies on heating the material [47].

Graphene possesses very high carrier concentrations and is predicted to achieve switching speeds of 200 GHz [40, 48], 500 GHz [49] and even 1 THz [50] depending on material quality, which supersedes the capabilities of other materials. Practically achieved switching speeds of 2.5 GHz for indium tin oxide and 50 GHz for graphene have been reported [40]. In a comparative study with other transparent conductors graphene was found to be superior with 97% transmittance and lowest sheet resistance values in the mid-infrared [51]. It was also shown to have lower power consumption compared to indium tin oxide [40].

Graphene has been used in a wide range of tunable meta-optical devices [52] including non-linear metasurfaces [53], absorbers and polarisers [54, 55] as well as wavefront control devices [56]. Graphene has also been proposed for use in non-tunable analogue optical computation

devices [57, 58]. Tunable analogue optical computation based on graphene has been proposed using multilayer thin-film stacks for operation in reflection [27]. While these structures are in principle versatile, their large -scale experimental implementation using graphene flakes can become very complex.

Graphene -coated subwavelength gratings and metasurfaces for analogue optical computation in transmission offer intriguing prospects for versatile devices at lower complexity. Graphene can be epitaxially grown on silicon carbide wafers as well as on silicon carbide on silicon pseudo-substrates [59-63]. In particular, the use of silicon carbide on silicon possesses the unique capability of selective coverage by graphene with high adhesion not possible with flake transfer methods [64]. The use of epitaxial graphene on silicon carbide offers a comparatively simple and experimentally scalable alternative. In addition, when combined with silicon carbide [65-68], graphene offers the possibility of engineering metasurfaces with tunable spatial computation capability for operation at mid-infrared wavelengths. The use of a zero-contrast grating design ensures continuous graphene coverage [69].

Here we computationally demonstrate that subwavelength zero-contrast gratings of silicon carbide covered with a monolayer of graphene enable electrically tunable, all-optical computation in the spatial domain at mid-infrared wavelengths. Specifically, we demonstrate that these devices permit high-pass spatial frequency filtering of transmitted wavefields that can be modified by changing the Fermi level of graphene. We provide numerical examples of this tuning capability by demonstrating a device that can be electrically switched between transmitting an edge-detected image and transmitting the original image with high fidelity. We further investigate the effects of geometrical parameters and the location of the graphene in the grating on the optical transfer function of the filter.

2. Graphene covered subwavelength gratings as spatial frequency filters

The system under consideration is shown in Figure 1. Light interacts with a transparent or opaque sample and the transmitted light then passes through a graphene coated zero contrast grating. The object could be located directly on the grating, an image of the object could be projected onto the grating or the grating could be positioned elsewhere in the optical system. There is no requirement for the grating to be placed in the Fourier plane.

After transmission through an object under study, a normally incident plane wave transforms into a complex wavefield which serves as an incident field $E_{in}(x,y)$ to a processing device, such as filter. Such a scalar incident electric field can be decomposed into a sum of plane waves travelling at different angles θ and φ and can be represented with $\tilde{E}_{in}(k_x,k_y)$ denoting the Fourier transform of the field. The spatial frequencies k_x and k_y are the components of the wave vector in the x- and y- direction respectively defined as $k_x = k_0 \cdot sin\theta \cdot cos\varphi$ and $k_y = k_0 \cdot sin\theta \cdot sin\varphi$, where $k_0 = 2\pi/\lambda_0$ and λ_0 is the free space wavelength of incident radiation. For φ=0° $cos\varphi$ =1 and $k_x = k_0 \cdot sin\theta$. Often normalised spatial frequency given as k_x/k_0 is used. The standard spherical coordinate system notation was used where θ is measured from the optical (z-) axis and φ is the azimuthal angle with respect to the x-z plane. Upon transmission of this field through the grating device with an angular dependent transmission $\tilde{t}(k_x,k_y)$, the transmitted field is given by $\tilde{E}_{out}(k_x,k_y) = \tilde{t}(k_x,k_y) \cdot \tilde{E}_{in}(k_x,k_y)$. Hence, the device permits spatial frequency filtering of a transmitted wavefield. As described in detail in [16], $\tilde{t}(k_x,k_y)$ is referred to as the optical transfer function (OTF) of the grating device. Here we demonstrate that the device under consideration can be tuned to suppress the transmission of low spatial frequencies and thereby performs edge-detection on transmitted images. Thanks to the tunable transmission characteristics $\tilde{t}(k_x,k_y,E_f)$ of the graphene coated grating, the OTF can be switched from high-pass filtering or 'filter on' mode to a transparent or 'filter off' mode.

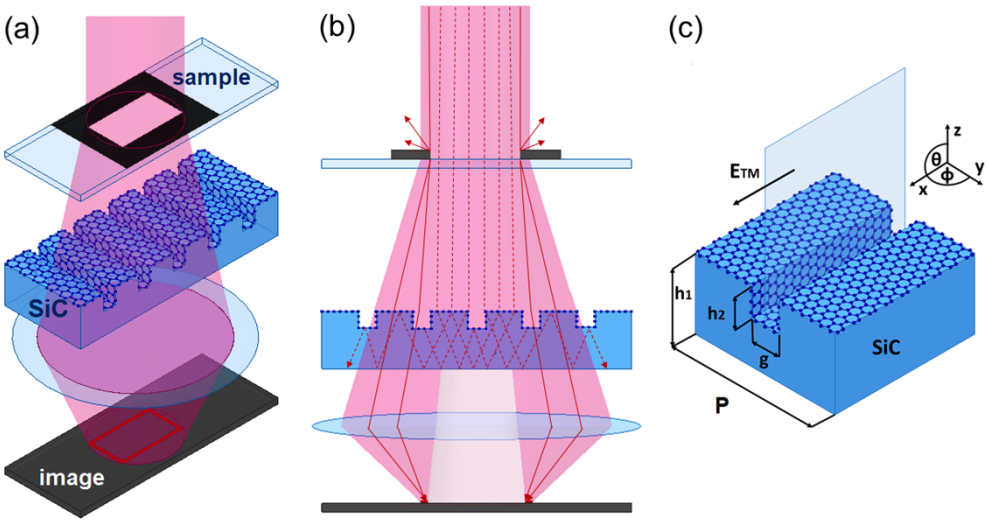

Fig.1.a) Schematic of imaging edge detection using SiC/ graphene grating. b) The grating acts as a spatial frequency filter where rays propagating at small angles from the flat part of the sample are trapped in the waveguiding SiC layer, while rays transmitted via curved edges are transmitted and focused by a lens forming edge-enhanced image. c) One period of the grating with P = 2 μm, g = 150 nm, h_1 = 980 nm, h_2 = 470 nm.

Spatial frequency filtering is achieved via coupling of normally incident radiation into a dielectric silicon carbide waveguide via a diffraction grating etched onto the waveguide. The periodicity of the grating is designed in a way that first-order diffracted beams (m = ±1) are phase matched to the TE waveguide mode. Once in the waveguide, the radiation propagates parallel to the surface in the form of guided mode and is eliminated from the radiation transmitted downwards towards the image plane. For larger angles of incidence, phase matching no longer holds for the grating and the efficiency of the coupling into the waveguide decreases, hence increasing the transmission.

Figure 1(c) shows the proposed spatial frequency filter based on a grating of graphene-coated silicon carbide illuminated with a plane wave mid-infrared electromagnetic field with a wavelength of 4 μm. The graphene coating is added to enable the dynamic tuning and switching of the device. A grating is inherently polarisation-dependent and, in this case, we assume that the incident electric field is oriented along the grating grooves in the x- direction. The plane of incidence is chosen as the x-z plane and thus the incident field is TM or p- polarised mode. This means that the angular dependence is calculated along the x axis or along the grating grooves.

SiC is a polar dielectric with optical constants that exhibit a complex dependence on wavelength, calculated using its transverse and longitudinal optical phonon resonances occurring at 12.55 μm and 10.28 μm [65-68]. The specific expression used in the modelling is provided in the supplemental document (Eq. S1). However, near 4 μm its dielectric properties vary only slowly and for the purpose of calculating guiding modes we take the refractive index to be n=2.482. The waveguide thickness h_1=980 nm was chosen such that it supports only the fundamental TE waveguide mode (E_x) with mode effective index n_{eff}=2.0 calculated using an effective height of h_{eff}=745 nm to account for the change in effective index of the guided mode due to the removal of some of the material to create the grating. Following the phase matching condition $n_{eff} = n_{inc} \cdot \sin\theta_{inc} - m \cdot \lambda_0 / p$ the chosen diffraction grating has a period of P=2 μm. The depth of the grating was chosen to be h_2=470 nm based on simulations indicating that deeper gratings provide better coupling.

Although commonly gratings with a filling fraction or duty cycle of 0.5 are used for coupling to resonant waveguide gratings, gap size can have a significant effect on the tunability of the device due to the modal field overlap with the graphene. Hence, gap sizes of 80, 150 and 500 nm, i.e., duty cycles of 0.04, 0.075 and 0.25 respectively, were considered in this investigation. We also study the effect of having full coverage of the gratings as well as the case of partial coverage where graphene is located on the top surface of the gratings and none inside the gaps. The addition of the graphene coating is expected to alter the optimum conditions for phase matching compared to the bare SiC waveguide.

The structure was simulated using a full-wave finite element method (FEM) in ANSYS Electronics Desktop [70]. Floquet ports were used at the top and bottom of the simulation area, which includes periodic boundaries along x- and y- directions containing one period of the grating. The Floquet port TM mode was used with orientation of the electric field parallel to the grating grooves, which represents plane electromagnetic wave illumination from the top in -z direction with specified θ and φ angles. The transmission and complex optical transfer functions were determined through the S-parameters.

Graphene was modelled as a 3D slab of 0.34 nm thickness and as a lossy wavelength dependent material with $\varepsilon(\omega)$ calculated from the Kubo formula for conductivity $\sigma(\omega)$ [27, 36], details of the formula and generated mesh are given in supplemental document (Eqs S2-S5, Fig.S1). A change in the Fermi level of graphene will alter its conductivity and optical properties, hence affecting the transmission through the grating. Here we compare Fermi levels of E_f=0.4eV and E_f=0.212eV of a p- type doped graphene, which are based on experimental literature values [32, 36, 71].

For edge -enhanced image formation using this device, key parameters are the contrast, effected by the minimum and maximum transmission at normal incidence vs other angles, the numerical aperture (the range of spatial frequencies that are modified by the grating), and the degree of tuning ΔT calculated as the difference in transmission at filter on and off states corresponding to the change in Fermi level at normal incidence at the operation wavelength. This tuning of transmission is a result of tuning of the resonance $\Delta\lambda$.

Figure 2(a) shows the transmission amplitude $|S_{21}|$ at normal incidence for gratings with the dimensions P = 2 μm, g = 150 nm, h_1 = 980 nm, h_2 = 470 nm for the 2 chosen Fermi levels of graphene. At a Fermi level of 0.4eV, a narrow deep resonance at 4.087 μm is found (slightly shifted from the intended 4 μm due to the addition of graphene), where the transmission is blocked. This 4.087 μm wavelength, where the transmission in minimum, is used as the operation wavelength of the filter (shown as black dotted line in Fig 2(a)). For a Fermi level of 0.212eV the resonance is broader and shallower and shifted to 4.098 μm. Due to the detuning of the resonance by 11 nm, the transmission at an operation wavelength of 4.087 μm changes from 0.13 to 0.72, providing a degree of tuning ΔT=0.59, thus achieving switching. The transmission through a bare SiC grating (without graphene) is also shown for comparison. It shows a resonance at 4.097 μm roughly as sharp and with a transmission minimum only marginally lower than the resonance with graphene at E_f=0.4eV. We conclude hence that the addition of graphene does not significantly degrade the overall SiC filtering performance, while adding tunability.

Figure 2(b) demonstrates the spatial frequency filtering operation and tuning at 4.087 μm. It shows the transmission of the device as a function of normalised spatial frequency, i.e., the magnitude of optical transfer function (OTF). The curve for E_f=0.4eV is obtained at resonance of 4.087 μm and represents the filter during operation or 'filter on', blocking a large fraction of normally incident radiation as well as rays incident at small angles up to 10.4°. The transmission

then gradually increases for larger spatial frequencies and can be well approximated by a linear function in the region between 0.05-0.18 k_x/k_0. The contrast, calculated as the difference between transmission values at k_x/k_0=0 and 0.18, is estimated as 0.47. For larger values k_x/k_0 up to 1.0 transmission reaches up to 99%, as observed in the supplemental document Figure S2a) and Figure 3 maps. The phase as a function of wavelengths and spatial frequency is available in supplemental document Figures S2, S3. The curve for E_f=0.212eV is detuned and corresponds to a 'filter off' operation with 72% transmission at normal incidence and low spatial frequencies. Transmittances defined as $T = |S_{21}|^2$, corresponding to the intensity of the transmitted radiation, are shown in the supplemental document Figure S4.

Figures 3(a) and (b) show the transmission as a function of both wavelength and normalised spatial frequency for E_f=0.4eV and E_f=0.212eV, respectively for the same grating with gap g = 150 nm. Due to the inverted scale, brighter colours indicate lower transmission. Resonances shift towards shorter wavelengths as k_x increases. For a Fermi level of E_f=0.4eV, a second mode appears from the angle of incidence of θ=11.2°, which corresponds to k_x/k_0=0.19, and for E_f =0.212eV a faint second mode appears starting from an angle of θ=15.2°, which corresponds to k_x/k_0=0.26. These second modes are not present at normal incidence. Alternative 1D plots versus wavelength for a select number of angles and showing both modes are available in the supplemental document Figure S5.

We compare the electric fields in the gratings at normal incidence in the maps in Figure 4 plotted at the resonant frequency corresponding to each configuration. The waveguide mode is observed in all gratings, with strong field along the centre of the SiC waveguide aligned to the x-axis and fringing fields outside. The SiC grating without graphene has the strongest field, followed by graphene covered grating with E_f=0.4eV and the weakest field in graphene grating with E_f=0.212eV. This trend is further confirmed by the vertical cross section plot of the electric field magnitude through the middle of the gap g = 150 nm as shown in Figure 5(a). This is consistent with the calculated absorbance $A = 1 - |S_{21}|^2 - |S_{11}|^2$ shown in (Figure 5(b)) for normal incidence. The graphene grating with E_f=0.212eV has the highest absorption, followed by the grating with E_f=0.4 eV and the lowest absorption is by the SiC grating without graphene. This is due to the presence of the lossy, conducting graphene. Note that operation of the filter is dominated by the guided mode resonance and its detuning due to the change in the optical properties of the material, rather than due to the absorption level of graphene itself.

As seen in Figure 4, due to the proximity to the centre of the waveguide, the fields are stronger near the bottom of the gap and weaker near the top. For this reason, it is essential to have the graphene also covering the sides and bottom of the gap, to enhance its interaction with the waveguide fields, which enhances tunability. Electric field magnitude line plots in the horizontal cross section are provided in supplemental document Figure S6. Indeed, Figure 6 compares the performance of the filter with 150 nm gap when using a full graphene coating versus partial coating only covering the top surfaces of the grating (Figure 6(a)) and OTF (Figure 6(b)). The fully-coated grating achieves a Δλ of 11 nm, considerably larger than the Δλ =2 nm for the grating with partial coating with no graphene in the gaps. This translates to a higher degree of tuning of the OTF for the fully-coated grating device by 0.23 at normal incidence.

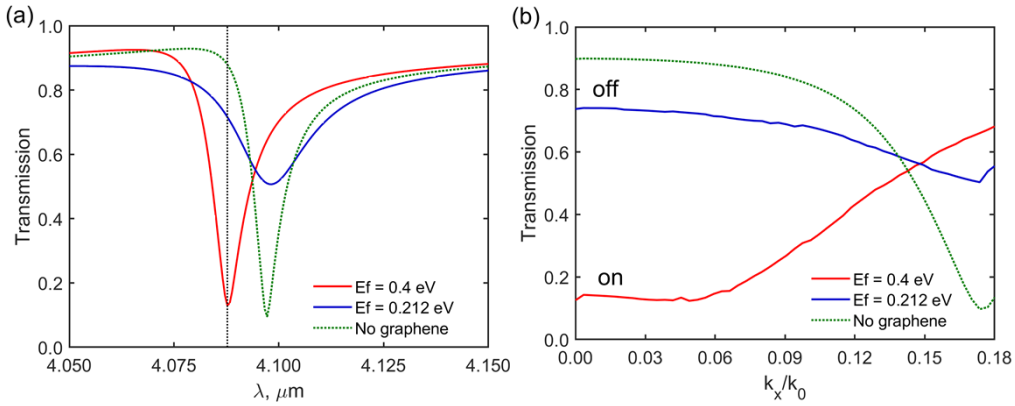

Fig.2. Transmission amplitude $|S_{21}|$ of SiC/graphene gratings for 2 different Fermi levels and g = 150 nm, in addition to a SiC grating without graphene (a) vs wavelength, (b) vs normalized spatial frequency at the resonant wavelength λ=4.087 μm corresponding to a Fermi level of 0.4eV.

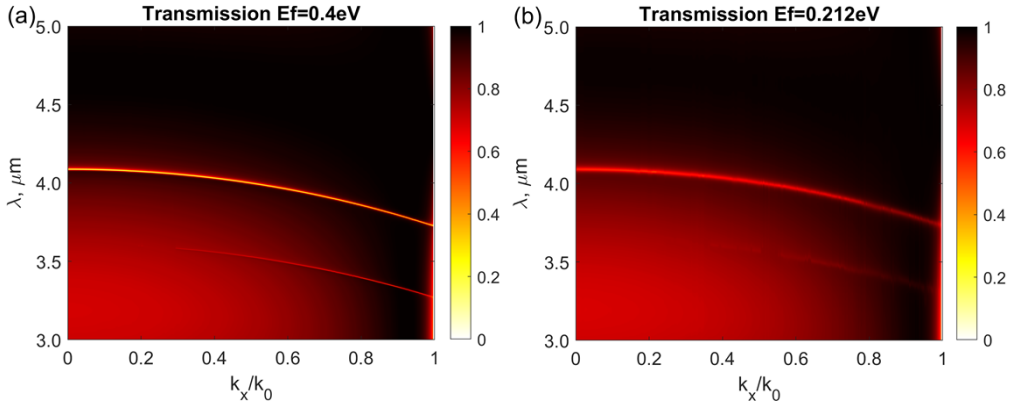

Fig.3.Transmission amplitude $|S_{21}|$ of SiC/graphene gratings with g = 150 nm for TM mode vs wavelengths and normalized spatial-frequencies at graphene Fermi levels a) Ef=0.4eV, b) Ef=0.212eV. Inverted scale is used where yellow indicates low transmission.

Finally, in order to guide the design of tunable spatial frequency filters, we have also conducted a parametric analysis of the fully covered grating to illustrate dependencies on the gap size. The optical response was simulated for additional gap sizes of 80 nm and 500 nm, while maintaining a period P=2 μm. Figure 7 compares the performance of gratings with gaps of 80, 150 and 500 nm. A grating with an 80 nm gap demonstrates good wavelength tunability of 8 nm and intermediate degree of tuning ΔT=0.43. For g=500nm gap the grating with graphene Fermi level of E_f=0.4eV achieves a near-zero transmission of 0.02, e.g. strong filtering of normally incident radiation, with a broader resonance and wavelength tunability of 9 nm. However, switching to E_f=0.212eV achieves a degree of tuning of only ΔT=0.16 compared to ΔT=0.6 for 150 nm gap at normal incidence due to the low transmission in the 'off' state. Individual plots for the transmission, phase and absorption for g=500nm gap are available in the supplemental document Figure S7.

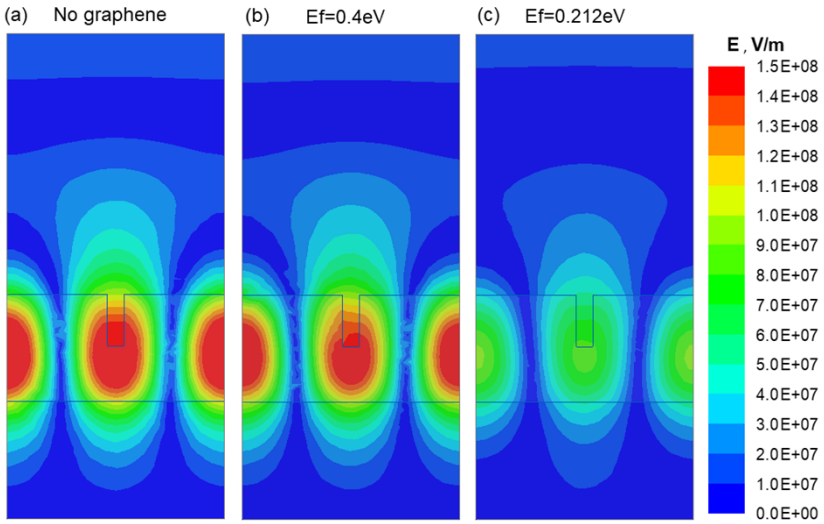

Fig.4. Magnitude of electric field in cross section across the grating with g = 150 nm at normal incidence a) SiC grating without graphene, b) SiC/graphene grating at Ef=0.4eV, c) SiC/graphene grating at Ef=0.212eV. Fields are plotted at individual resonant frequencies for each condition.

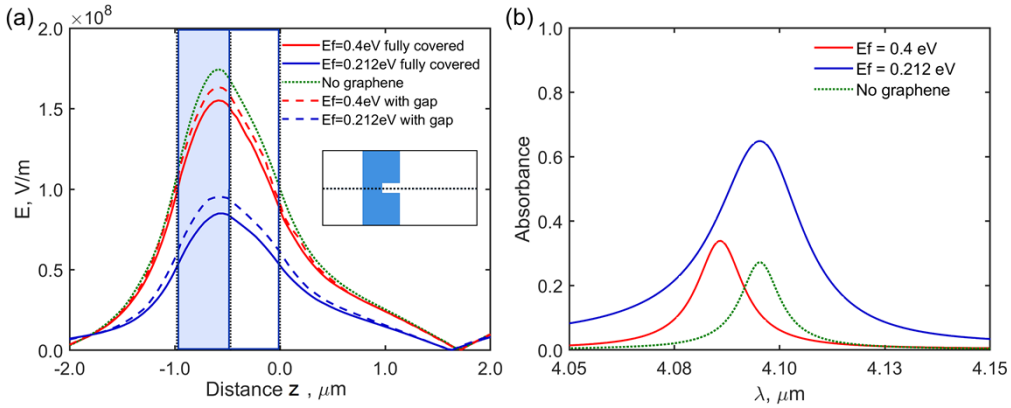

Fig.5. Magnitude of electric field in cross sections of SiC/graphene grating with g = 150 nm a) vertical through the centre of the gap with blue rectangle indicating location of the SiC followed by the grating gap, b) absorbance of SiC/graphene grating vs Fermi level, including grating without graphene. Fields are plotted at individual resonant frequencies for each condition.

Thus, gap size has a significant effect on tunability and operational parameters of the filter. There is a trade-off between suppression of transmission at normal incidence, contrast and degree of tuning between the filter on and off states. A grating with a 150 nm gap offers a good compromise on minimum transmission values affecting contrast and offers best wavelength tunability of 11 nm and degree of tuning ΔT=0.6, a 0.17 improvement over 80 nm gap and 0.44 over 500 nm gap. Also, it can be seen from Figure 7(b) that gap size is a critical parameter for changing the numerical aperture of the filter with 80, 150 and 500 nm gap gratings estimated to have numerical apertures of 0.15, 0.18 and 0.45 based on the deviation of linear fit from the transmission versus normalised spatial frequency curves (see plots of the fit in supplemental material Figure S8). These numerical apertures correspond to filtering out the rays to incident angles up to 8.6°, 10.4° and 26.7° correspondingly. Within these ranges, the distortions to the image would be minimal. The plots of transmission versus angle of incidence versus different gap sizes are available in the supplemental document, Figure S9.

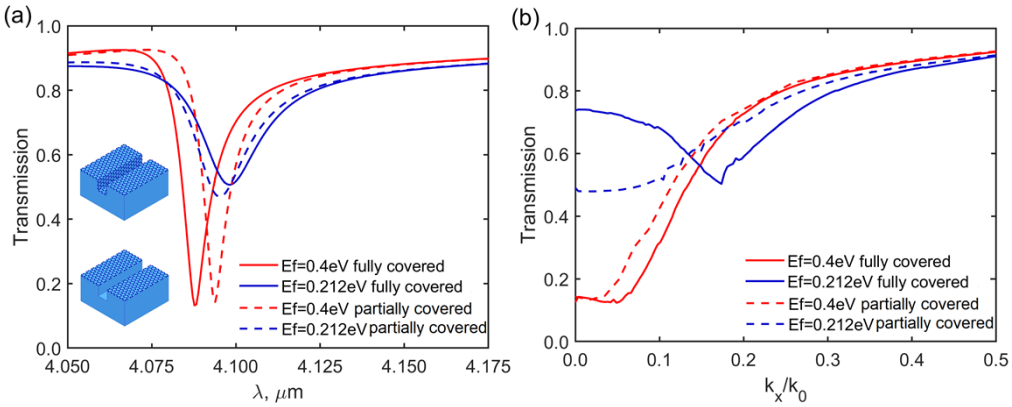

Fig.6. Comparison of transmission amplitude $|S_{21}|$ of SiC/graphene grating with g = 150 nm vs Fermi level for different graphene coverage a) vs wavelength, b) vs angle of incidence, solid curves are at the resonant wavelength corresponding to Fermi level of 0.4eV for fully covered grating, dashed curves are at the resonant wavelength corresponding to Fermi level of 0.4eV for partially covered grating.

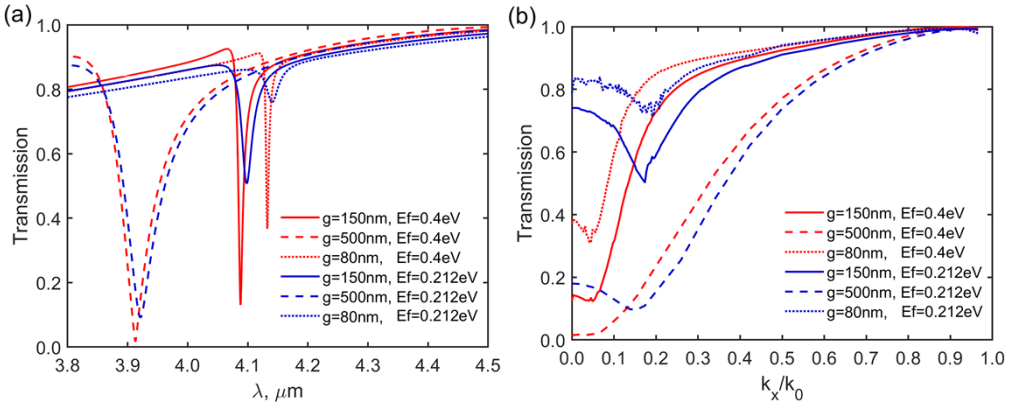

Fig.7. Transmission amplitude $|S_{21}|$ of SiC/graphene grating vs Fermi level for different gaps a) vs wavelength, b) vs normalized spatial frequency, all curves are at the resonant wavelength corresponding to Fermi level of 0.4eV for each gap size.

The grating is also sensitive to TE illumination across the grooves as shown in the supplemental document Figure S10 with a resonance at shorter wavelength. However, the dimensions of the grating are not optimised for operation as a filter at that wavelength. Square or rectangular arrays could be investigated to permit operation in two dimensions and add polarisation sensitivity. Different operations could be performed at different wavelengths utilising different polarisations.

3. Edge detection application

Image processing with the graphene covered grating was simulated by modelling the device as a space-invariant linear optical system. This permits calculation of the Fourier transform of a transmitted image by multiplication of the Fourier transform of the incident image with the optical transfer function (OTF) of the device. The theoretical framework for this is described in detail in [17]. Here, we use the complex transmission coefficient S_{21} as the OTF of the system.

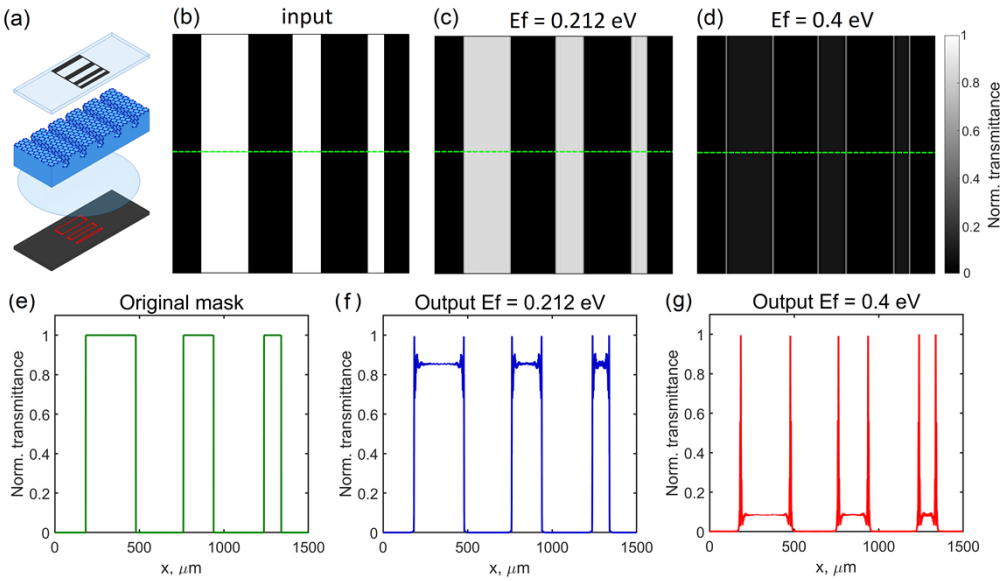

Fig.8. Demonstration of a dynamically tunable all-optical edge-detection of a transmitted amplitude image using the fully graphene covered SiC grating with gap of 150 nm at λ = 4.087 μm for TM polarised incident light. (a) Schematic of edge detection using SiC/ graphene grating, (b) original sample, (c) transmitted image obtained in 'transparent' or 'filter off' mode for Ef=0.212eV, (d) transmitted image obtained in 'edge detection' or 'filter on' mode for Ef=0.4eV. Normalised transmittance $T = |S_{21}|^2$ along the dotted green lines shown in (b-d) for (e) original mask, (f) 'filter off' mode, (g) 'edge detection' mode.

Figure 8 shows the numerical modelling of the switching operation of the SiC/graphene grating filter for all-optical real-time image processing. An amplitude mask in a form of a grating with three slits and total object size of 1500 μm was used as a sample (Figure 8(b, e)). In the transparent or 'filter off' mode, corresponding to the graphene Fermi level of 0.212eV, the incident image is transmitted relatively unchanged, except for the introduction of minor artefacts (Figure 8(c)). In the 'filter on' mode, corresponding to graphene Fermi level of 0.4eV, narrow spikes of intensity reveal the sample edges as seen in Figure 8(d). Figures 8(e-g) shows the normalised transmittance $T = |S_{21}|^2$ or intensity of the detected radiation plotted along the line across the sample and images (green dots). The maximum transmittance in the 'filter off' state (Figure 8(f)) is determined by the infrared properties of the SiC waveguide material. Very narrow lines of high transmission are seen at the locations corresponding to the edges of the sample, in line with the abrupt change in amplitude near the image edges (Figure 8(g)). The residual transmittance when the filter is on is determined by the quality of the guided mode resonance.

4. Conclusion

Ultra-compact and dynamically tunable meta-optical devices are important for real-time computation in the spatial domain, image processing and wavefront sensing due to increased processing speed, data throughput and miniaturisation. Here we proposed a SiC/graphene grating based mid-infrared spatial frequency filter which can be electrically tuned via change in graphene Fermi level. We demonstrated that the high-pass filter permits first-order spatial differentiation of the transmitted wavefields that can be switched on and off. We demonstrated numerical switching between transmitting an edge-detected image and transmitting the original image unchanged. Change in the graphene Fermi level from 0.4 to 0.212eV altered its

conductivity and detuned the resonance by 11 nm leading to a 60% transmission change between on and off states.

We investigated the effect of graphene location and coverage using gratings fully and partially covered with graphene. The proximity of graphene to the region with the strongest field, such as near the bottom of the grating gaps, allows for enhanced tunability, hence indicating that a fully conformal graphene coverage capability plays a crucial role. This can be easily achieved with epitaxial growth of graphene on SiC. We also investigated the effect of the grating dimensions on tunability and found that varying the gap width enables tuning of transmission levels to the application requirements and allows for the selection of the numerical aperture of the filter device. Finally, we have numerically demonstrated the use of the filter by dynamically switching on and off the edge detection using a three slit grating object.

Further exploration of phonon-plasmon coupling occurring at longer wavelength offers even more options for tailored optical transfer function design and tuning. Graphene has potential to enable ultrafast high-throughput real-time tunable processing of optical data in compact mid-infrared devices.

Funding

This research was funded by the Commonwealth of Australia, represented by the Australian Research Council through the Centre of Excellence for Transformative Meta-Optical Systems (CE200100010)

Disclosures

The authors declare that there are no conflicts of interest.

Data availability. Data underlying the results presented in this paper are not publicly available at this time but may be obtained from the authors upon reasonable request.

Supplemental document. See Supplement 1 for supporting content

References

1. J. J. Cadusch, J. Meng, B. J. Craig, V. R. Shrestha and K. B. Crozier, "Visible to long-wave infrared chip-scale spectrometers based on photodetectors with tailored responsivities and multispectral filters," Nanophotonics, **9**(10), 3197-3208 (2020).
2. S. Türker-Kaya and C. W. Huck, "A review of mid-infrared and near-infrared imaging: principles, concepts and applications in plant tissue analysis," Molecules **22**, 168 (2017).
3. E. Kontsek, A. Pesti, M. Björnstedt, T. Üveges, E. Szabó, T. Garay, P. Gordon, S. Gergely, and A. Kiss, "Mid-infrared imaging is able to characterize and separate cancer cell lines," Pathol. & Oncol. Res. **26**, 2401–2407 (2020).
4. Y. He, B. Deng, H. Wang, L. Cheng, K. Zhou, S. Cai, and F. Ciampa, "Infrared machine vision and infrared thermography with deep learning: A review," Infrared Physics & Technology **116**, 103754 (2021).
5. C. Kuenzer and S. Dech, "Thermal infrared remote sensing," Remote. Sens. Digit. Image Process **10**, 978–94 (2013).
6. M. Chi, A. Plaza, J. A. Benediktsson, Z. Sun, J. Shen, and Y. Zhu, "Big data for remote sensing: Challenges and opportunities," Proc. IEEE **104**, 2207–2219 (2016).
7. T. Zhu, Y. Zhou, Y. Lou, H. Ye, M. Qiu, Z. Ruan, and S. Fan, "Plasmonic computing of spatial differentiation," Nat. Commun. **8**, 1–6 (2017).
8. T. Zhu, Y. Lou, Y. Zhou, J. Zhang, J. Huang, Y. Li, H. Luo, S. Wen, S. Zhu, Q. Gong et al., "Generalized spatial differentiation from the spin hall effect of light and its application in image processing of edge detection," Phys. Rev. Appl. **11**, 034043 (2019).
9. L. Wesemann, E. Panchenko, K. Singh, E. Della Gaspera, D. E. Gómez, T. J. Davis, and A. Roberts, "Selective near-perfect absorbing mirror as a spatial frequency filter for optical image processing," APL Photonics **4**, 100801 (2019).
10. T. Zhu, C. Guo, J. Huang, H. Wang, M. Orenstein, Z. Ruan, and S. Fan, "Topological optical differentiator," Nat. Commun. **12**, 1–8 (2021).

11. D. A. Bykov, L. L. Doskolovich, A. A. Morozov, V. V. Podlipnov, E. A. Bezus, P. Verma, and V. A. Soifer, "First-order optical spatial differentiator based on a guided-mode resonant grating," Opt. Express **26**, 10997–11006 (2018).
12. A. Cordaro, H. Kwon, D. Sounas, A. F. Koenderink, A. Alù, and A. Polman, "High-index dielectric metasurfaces performing mathematical operations," Nano Lett. **19**, 8418–8423 (2019).
13. L. Wesemann, J. Rickett, J. Song, J. Lou, E. Hinde, T. J. Davis, and A. Roberts, "Nanophotonics enhanced coverslip for phase imaging in biology," Light. Sci. & Appl. **10**, 1–6 (2021).
14. Y. Zhou, H. Zheng, I. I. Kravchenko, and J. Valentine, "Flat optics for image differentiation," Nat. Photonics **14**, 316–323 (2020).
15. L. Wesemann, J. Rickett, T. J. Davis, and A. Roberts, "Real-time phase imaging with an asymmetric transfer function metasurface," ACS Photonics **9**, 1803–1807 (2022).
16. C. Guo, M. Xiao, M. Minkov, Y. Shi, and S. Fan, "Photonic crystal slab Laplace operator for image differentiation," Optica **5**, 251–256 (2018).
17. L. Wesemann, T. J. Davis, and A. Roberts, "Meta-optical and thin film devices for all-optical information processing," Appl. Phys. Rev. **8**, 031309 (2021).
18. F. Zangeneh-Nejad, D. L. Sounas, A. Alù, and R. Fleury, "Analogue computing with metamaterials," Nat. Rev. Mater. **6**, 207–225 (2021).
19. Y. Park, C. Depeursinge, and G. Popescu, "Quantitative phase imaging in biomedicine," Nat. Photonics **12**, 578–589 (2018).
20. F. Rigaut, J. Cuby, M. Caes, J. Monin, M. Vittot, J. Richard, G. Rousset, and P. Lena, "Visible and infrared wavefront sensing for astronomical adaptive optics," Astron. Astrophys. **259**, L57–L60 (1992).
21. B. Vohnsen and D. Valente, "Surface-plasmon-based wavefront sensing," Optica **2**, 1024–1027 (2015).
22. Y. Zhang, C. Fowler, J. Liang, B. Azhar, M. Y. Shalaginov, S. Deckoff-Jones, S. An, J. B. Chou, C. M. Roberts, V. Liberman, M. Kang, C. Ríos, K. A. Richardson, C. Rivero-Baleine, T. Gu, H. Zhang, and J. Hu, "Electrically reconfigurable non-volatile metasurface using low-loss optical phase-change material," Nat. Nanotechnol. **16**, 661–666 (2021).
23. E. Arbabi, A. Arbabi, S. M. Kamali, Y. Horie, M. Faraji-Dana, and A. Faraon, "Mems-tunable dielectric metasurface lens," Nat. Commun. **9**, 1–9 (2018).
24. P. C. Thrane, C. Meng, F. Ding, and S. I. Bozhevolnyi, "Mems tunable metasurfaces based on gap plasmon or Fabry–Pérot resonances," Nano Lett. **22**, 6951–6957 (2022).
25. C. Meng, P. C. Thrane, F. Ding, and S. I. Bozhevolnyi, "Full-range birefringence control with piezoelectric mems-based metasurfaces," Nat. Commun. **13**, 1–7 (2022).
26. V. Iushkov, A. Shorokhov, and A. Fedyanin, "Tunable GaAs metasurfaces for ultrafast image processing," in Journal of Physics: Conference Series, vol. 2015 (IOP Publishing, 2021), p. 012057.
27. A. Momeni, K. Rouhi, and R. Fleury, "Switchable and simultaneous spatiotemporal analog computing with computational graphene-based multilayers," Carbon **186**, 599–611 (2022).
28. X. Zhang, Y. Zhou, H. Zheng, A. E. Linares, F. C. Ugwu, D. Li, H.-B. Sun, B. Bai, and J. G. Valentine, "Reconfigurable metasurface for image processing," Nano Lett. **21**, 8715–8722 (2021).
29. G. Chen, J. Zhou, S. E. Bopp, J. Zhao, and Z. Liu, "Visible and near-infrared dual band switchable metasurface edge imaging," Opt. Lett. **47**, 4040–4043 (2022).
30. T. Xiao, H. Yang, Q. Yang, D. Xu, R. Wang, S. Chen, and H. Luo, "Realization of tunable edge-enhanced images based on computing metasurfaces," Opt. Lett. **47**, 925–928 (2022).
31. F. Bonaccorso, Z. Sun, T. Hasan, and A. Ferrari, "Graphene photonics and optoelectronics," Nat. Photonics **4**, 611–622 (2010).
32. K. S. Novoselov, V. I. Fal'ko, L. Colombo, P. R. Gellert, M. G. Schwab and K. Kim, "A roadmap for graphene," Nature **490**, 192-200 (2012).
33. A. Grigorenko, M. Polini and K. Novoselov, "Graphene plasmonics," Nat. Photonics **6**, 749 (2012).
34. T. Low and P. Avouris, "Graphene plasmonics for terahertz to mid-infrared applications," ACS Nano **8**, 1086-1101 (2014).
35. F. J. Garcia de Abajo, "Graphene plasmonics: challenges and opportunities," ACS Photonics **1**, 135-152 (2014).
36. Y. Francescato, V. Giannini, and S.A. Maier, "Strongly confined gap plasmon modes in graphene sandwiches and graphene-on-silicon," New J. of Physics **15**, 063020 (2013).
37. L. Ju, B. Geng, J. Horng, C. Girit, M. Martin, Z. Hao, H. A. Bechtel, X. Liang, A. Zettl, Y. R. Shen and F. Wang, "Graphene plasmonics for tunable terahertz metamaterials," Nat. Nanotech., **6**(10), 630-634 (2011).
38. N. K. Emani, T. F. Chung, A. V. Kildishev, V. M. Shalaev, Y. P. Chen and A. Boltasseva, "Electrical modulation of fano resonance in plasmonic nanostructures using graphene," Nano Lett., **14**(1), 78-82 (2014).
39. E. Feigenbaum, K. Diest and H. A. Atwater, "Unity-order index change in transparent conducting oxides at visible frequencies," Nano Lett., **10**(6), 2111-2116 (2010).
40. G. Sinatkas, T. Christopoulos, O. Tsilipakos and E. E. Kriezis, "Comparative study of silicon photonic modulators based on transparent conducting oxide and graphene," Phys. Rev. Appl., **12**(6), 064023, (2019).
41. S. Basu, B. J. Lee and Z. M. Zhang, "Infrared radiative properties of heavily doped silicon at room temperature," J. of Heat Transfer, **132**(2), 1-8 (2010).
42. S. Laux, N. Kaiser, A. Zöller, R. Götzelmann, H. Lauth and H. Bernitzki, "Room-temperature deposition of indium tin oxide thin films with plasma ion-assisted evaporation," Thin Solid Films, **335**(1-2), 1-5 (1998).
43. Y. Wang, A. C. Overvig, S. Shrestha, R. Zhang, R. Wang, N. Yu and L. D. Negro, "Tunability of indium tin oxide materials for mid-infrared plasmonics applications," Opt. Mat. Express, **7**(8), 2727-2739 (2017).

44. X. Liu, J. Park, J. H. Kang, H. Yuan, Y. Cui, H. Y. Hwang and M. L. Brongersma, "Quantification and impact of nonparabolicity of the conduction band of indium tin oxide on its plasmonic properties," Appl. Phys. Letts, **105**(18), 181117, (2014).
45. A. Tamanai, T. D. Dao, M. Sendner, T. Nagao and A. Pucci, "Mid-infrared optical and electrical properties of indium tin oxide films," Physica Status Solidi (A) Applications and Materials Science, **214**(3), 1600467, (2017).
46. T. Kang, Z. Ma, J. Qin, Z. Peng, W. Yang, T. Huang, S. Xian, S. Xia, W. Yan, Y. Yang, Z. Sheng, J. Shen, C. Li, L. Deng and L. Bi, "Large scale, power-efficient Au/VO_2 active metasurfaces for ultrafast optical modulation" Nanophotonics **10**(2), 909–918, (2021).
47. M. Sadeghi, B. Janjan, M. Heidari and D. Abbott, "Mid-infrared hybrid Si/VO_2 modulator electrically driven by graphene electrodes," Opt. Express, **28**(7), 9198-9207 (2020).
48. T. Limmer, J. Feldmann and E. Da Como, "Carrier lifetime in exfoliated few-layer graphene determined from intersubband optical transitions," Phys. Rev. Lett., **110**(21), 217406, (2013).
49. M. Liu, X. Yin, E. Ulin-Avila, B. Geng, T. Zentgraf, L. Ju, F. Wang and X. Zhang, "A graphene-based broadband optical modulator," Nature, **474**(7349), 64-67 (2011).
50. L. Liao, J. Bai, R. Cheng, Y. C. Lin, S. Jiang, Y. Qu, Y. Huang and X. Duan, "Sub-100 nm channel length graphene transistors," Nano Lett., **10**(10), 3952-3956 (2010).
51. F. G. Micallef, P. K. Shrestha, D. Chu, K. McEwan, G. Rughoobur, T. Carey, N. Coburn, F. Torrisi, O. Txoperena and A. Zurutuza, "Transparent conductors for mid-infrared liquid crystal spatial light modulators," Thin Solid Films, **660**, 411-420 (2018).
52. J. Cheng, F. Fan, and S. Chang, "Recent progress on graphene-functionalized metasurfaces for tunable phase and polarization control," Nanomaterials **9**, 398 (2019).
53. D. A. Smirnova, A. E. Miroshnichenko, Y. S. Kivshar, and A. B. Khanikaev, "Tunable nonlinear graphene metasurfaces," Phys. Rev. B **92**, 161406 (2015).
54. A. Fallahi and J. Perruisseau-Carrier, "Design of tunable biperiodic graphene metasurfaces," Phys. Rev. B **86**, 195408 (2012).
55. P. C. Wu, N. Papasimakis, and D. P. Tsai, "Self-affine graphene metasurfaces for tunable broadband absorption," Phys. Rev. Appl. **6**, 044019 (2016).
56. H. Cheng, S. Chen, P. Yu, W. Liu, Z. Li, J. Li, B. Xie, and J. Tian, "Dynamically tunable broadband infrared anomalous refraction based on graphene metasurfaces," Adv. Opt. Mater. **3**, 1744–1749 (2015).
57. F. Zangeneh-Nejad and A. Khavasi, "Spatial integration by a dielectric slab and its planar graphene-based counterpart," Opt. Lett. **42**, 1954–1957 (2017).
58. Y. Fang, Y. Lou, and Z. Ruan, "On-grating graphene surface plasmons enabling spatial differentiation in the terahertz region," Opt. Lett. **42**, 3840–3843 (2017).
59. N. Mishra, M. Bosi, F. Rossi, G. Salviati, J. Boeckl and F. Iacopi, "Growth of graphitic carbon layers around silicon carbide nanowires," J. Appl. Phys. **126**, 065304 (2019).
60. N. Mishra, J. Boeckl, N. Motta and F. Iacopi, "Graphene growth on silicon carbide: A review," Phys. Status Solidi A **213**, 2277-2289 (2016).
61. F. Iacopi, N. Mishra, B. V. Cunning, D. Goding, S. Dimitrijev, R. Brock, R. H. Dauskardt, B. Wood and J. Boeckl, "A catalytic alloy approach for graphene on epitaxial SiC on silicon wafers," J. Mater. Res. 30, 609-616 (2015).
62. B. V. Cunning, M. Ahmed, N. Mishra, A. R. Kermany, B. Wood and F. Iacopi, "Graphitized silicon carbide microbeams: Wafer-level, self-aligned graphene on silicon wafers," Nanotechnology, **25**(32), 325301, (2014).
63. N. Mishra, S. Jiao, A. Mondal, Z. Khan, J. J. Boeckl, K. D. Gaskill, R. E. Brock, R. H. Dauskardt and F. Iacopi. "A graphene platform on silicon for the Internet of Everything". in 2018 IEEE Electron Devices Technology and Manufacturing Conference, EDTM 2018 - Proceedings. 211-213 (2018).
64. P. Bøggild, D. M. A. Mackenzie, P. R. Whelan, D. H. Petersen, J. D. Buron, A. Zurutuza, J. Gallop, L. Hao and P. U. Jepsen, "Mapping the electrical properties of large-area graphene," 2D Materials, **4**(4), 042003, (2017).
65. J. D. Caldwell, L. Lindsay, V. Giannini, I. Vurgaftman, T. L. Reinecke, S. A. Maier and O. J. Glembocki, "Low-loss, infrared and terahertz nanophotonics using surface phonon polaritons," Nanophotonics **4**, 44-68 (2015).
66. P. Rufangura, T. G. Folland, A. Agrawal, J. D. Caldwell and F. Iacopi, "Towards low- loss on-chip nanophotonics with coupled graphene and silicon carbide: a review, "J. Phys. Mater. **3**, 032005 (2020).
67. P. Rufangura, I. Khodasevych, A. Agrawal, M. Bosi, T. G. Folland, J. D. Caldwell and F. Iacopi, "Enhanced absorption with graphene-coated silicon carbide nanowires for mid-infrared nanophotonics," Nanomaterials **11**, 2339 (2021).
68. I. Khodasevych, P. Rufangura, and F. Iacopi, "Designing concentric nanoparticles for surface-enhanced light-matter interaction in the mid-infrared," Opt. Express **30**, 24118–24131 (2022).
69. R. Magnusson, "Wideband reflectors with zero-contrast gratings," Opt. Lett., **39**(15), 4337-4340 (2014).
70. Ansys Electronics Desktop, https://www.ansys.com/products/electronics.
71. A. Pradeepkumar, M. Amjadipour, N. Mishra, C. Liu, M. S. Fuhrer, A. Bendavid, F. Isa, M. Zielinski, H. I. Sirikumara, T. Jayasekara, D. K. Gaskill and F. Iacopi, "p-type epitaxial graphene on cubic silicon carbide on silicon for integrated silicon technologies," ACS Appl. Nano Mater. **3**, 830-841 (2019).